Residual-moveout-based WEMVA: A WAZ field data example - Part I

Yang Zhang and Biondo Biondi

ABSTRACT

In our previous reports (SEP–147 and SEP–149), we have laid the theoretic foundation of the residual-moveout-based wave-equation migration velocity analysis, and we present the test results on the synthetic 2-D BP model. In this paper, we report our efforts on applying this method to an industry scale 3-D marine WAZ data set — E-Octopus III in the Gulf of Mexico. The 3-D field data poses many challenges for our implementation, including irregular geometry, abnormal traces, complex 3-D salt geometry and more importantly, huge data volume and large domain dimensions. To overcome these hurdles, we apply careful data regularization and preprocessing, and employ a target-oriented inversion scheme, focusing on the update of sediment velocities in a subsalt region. This target-oriented scheme significantly reduces the computational cost, allowing us to keep the total computation load manageable on our academic cluster. Our preliminary result shows that, even though the angles of illumination on the subsalt sediments are very limited (does not exceed 25 degrees) in this data set, the moveout on the angle gathers are still measurable, therefore can be used for the RMO-based WEMVA update.

INTRODUCTION

Wave-equation migration velocity analysis (WEMVA) is a reflection tomography method which uses wave-equation rather than ray-based model to retrieve the velocity model from seismic data(Chavent and Jacewitz, 1995; Biondi and Sava, 1999). The velocity information comes from the seismic data redundancy that each reflector point in the subsurface is illuminated by wave energy from multiple directions. WEMVA exploits such redundancy by forming common-image gathers and then enforcing coherence among the common-image gathers to improve the velocity model.

We recently proposed the RMO-based WEMVA (Zhang et al., 2012), which describes the unflatness in the angle-domaincommon image gathers(ADCIGs) using residual-moveout (RMO). The method then tries to improve the velocity model based on the moveout information.

Previously, we have shown the successful application of RMO-based WEMVA on the 2-D BP synthetic model (Zhang et al., 2013). While the theory of this method can be easily extended to 3-D (Zhang and Biondi, 2012), a realistic 3-D data application remains very challenging. In this paper, we document the work flow of applying the RMO-based WEMVA on a Wide-Azimuth (WAZ) field data set. We illustrate the practical problems we encountered, and describes our measures to overcome/mitigate these problems so as to obtain the final WEMVA result in a timely manner.

E-OCTOPUS III WAZ DATA SET OVERVIEW

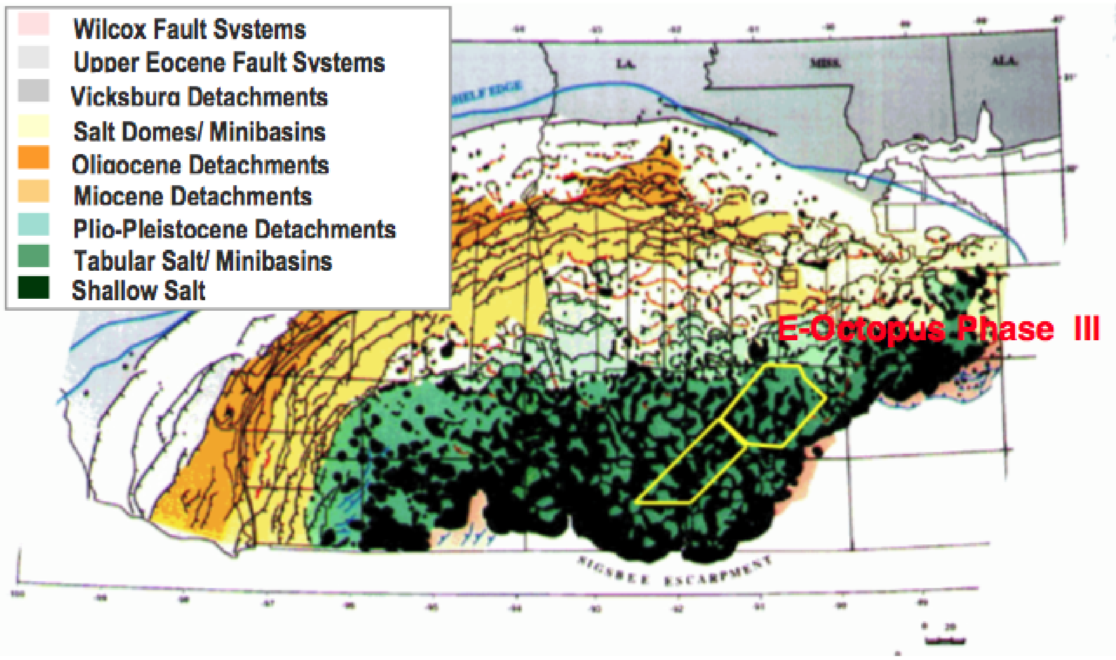

Figure 1: The structural summary map of the northern Gulf of Mexico, with the E-Octopus III survey area highlighted. Courtesy of Schlumberger. [**NR**]

The data set we examine in this report is a WAZ streamer survey acquired offshore Gulf of Mexico (GOM) by Schlumberger. Our portion of the data belongs to the "E-Octopus phase III" survey in the Green Canyon area. The corresponding survey area is about 35 km by 30 km (inline by cross-line).

Figure 1 shows the geological structure map of the Northern Gulf of Mexico, with our survey area marked. The processing report from Schlumberger describes the complex geological settings in this area:

> "The E-Octopus Phase III survey lies primarily in the Green Canyon protraction areas of the MMS Central Planning Area in the Gulf of Mexico. The northern Gulf of Mexico is a geologically complex basin resulting from interaction and deformation of salt and overlying sediment layers over geologic time. The geology around the survey area is characterized by extensive salt sheets with intervening deep-water sediment-filled

> mini-basins. The salt canopy is characterized by simple to complex salt features, some of which have thicknesses up to 30,000 ft and some that are extremely shallow, i.e. just under the water bottom. ”

Acquisition settings

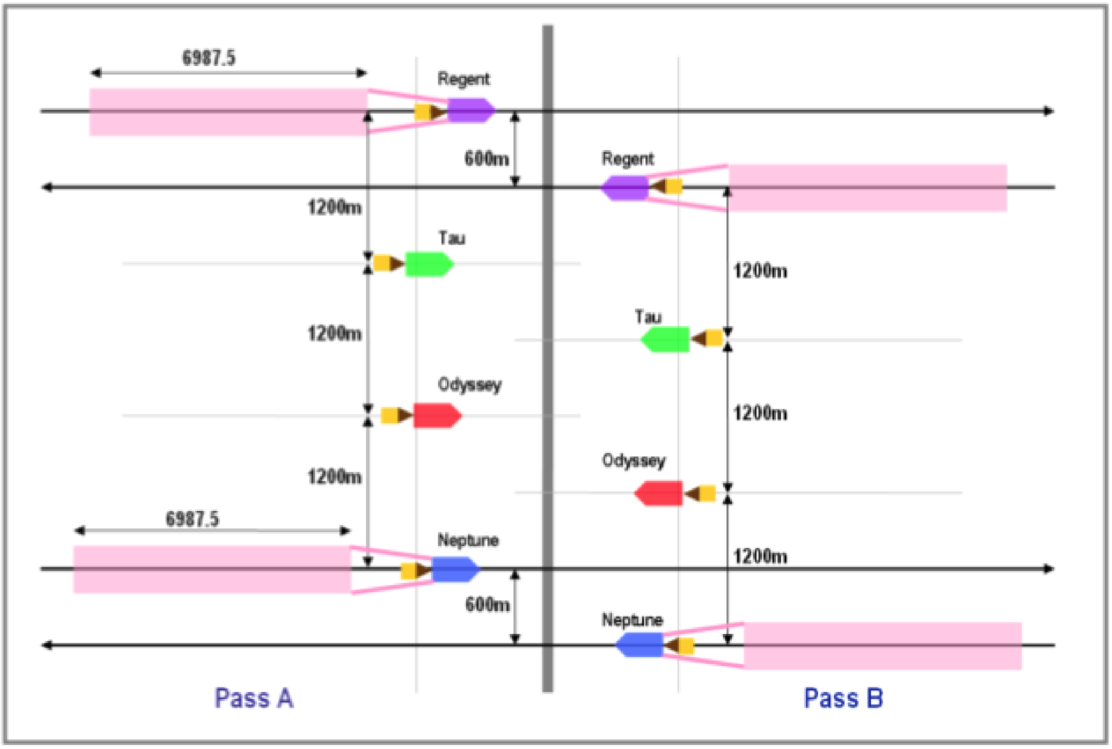

Figure 2: The nominal shooting configuration of this WAZ survey. Courtesy of Schlumberger. [**NR**]

The survey uses 4 marine seismic vessels simultaneously to achieve a wide-azimuth acquisition pattern. All 4 vessels act as sources but only 2 vessels tow receiver cables. The shooting/towing direction is from SW to NE (pass A) and vice versa (pass B). Figure 2 shows the nominal shooting configuration. The source positions are spaced every 150 m inline and 600 m crossline. The receiver streamers are only ∼7 km long; the receiver spacing is 12.5 m. The crossline spacing between neighboring streamers is 100 m. Figure 4(a) and 4(b) shows the total source and receiver coverages. From the shot locations map, we can easily identify the two types of sail-lines (pass A and pass B) in opposite directions.

The full span of crossline offset is [-4.2 km, +4.2 km], compared to the span of inline offset being [-7 km, 0] (pass A) or [0, +7 km] (pass B). Figure 3 illustrates the fold coverage map for a typical midpoint location (Rose diagram) under the nominal acquisition model. We can see that the survey illuminated at least 60° (out of 180°)

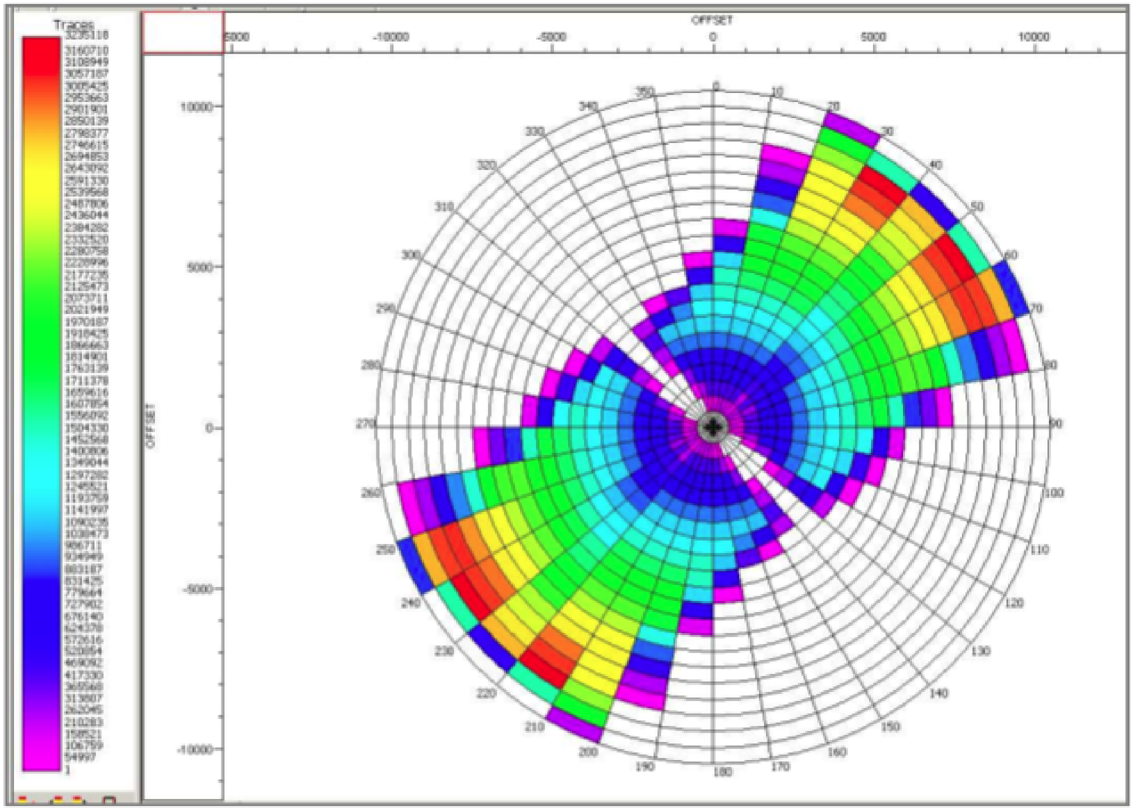

Figure 3: Rose Diagram showing fold by azimuth and offset under the nominal acquisition model. Courtesy of Schlumberger. [**NR**]

of azimuth range. Given the highly complex geology in the area, the wide azimuth coverage is a big advantage in terms of dealing with severe 3-D wave propagation effects compared with the old conventional narrow azimuth acquisition setup.

GEOMETRY PROCESSING

To process the geometry, we rotate and translate our processing grid to align x-axis with the inline direction and y-axis with the crossline direction. Figure 5 shows the shot locations map after the geometric transform.

The size of the original seismic data we receive is over 10 TB, containing over 72,000 shots. Our computational infrastructure is not able to handle a data set at this huge scale in its original form. To reduce the size of data, as well as the computational cost required to process this data, we take several measures during the data regularization.

- We regularize the data by binning them into two sets of regularly spaced data grids (one for pass A shotlines and one for pass B shotlines). The data grids

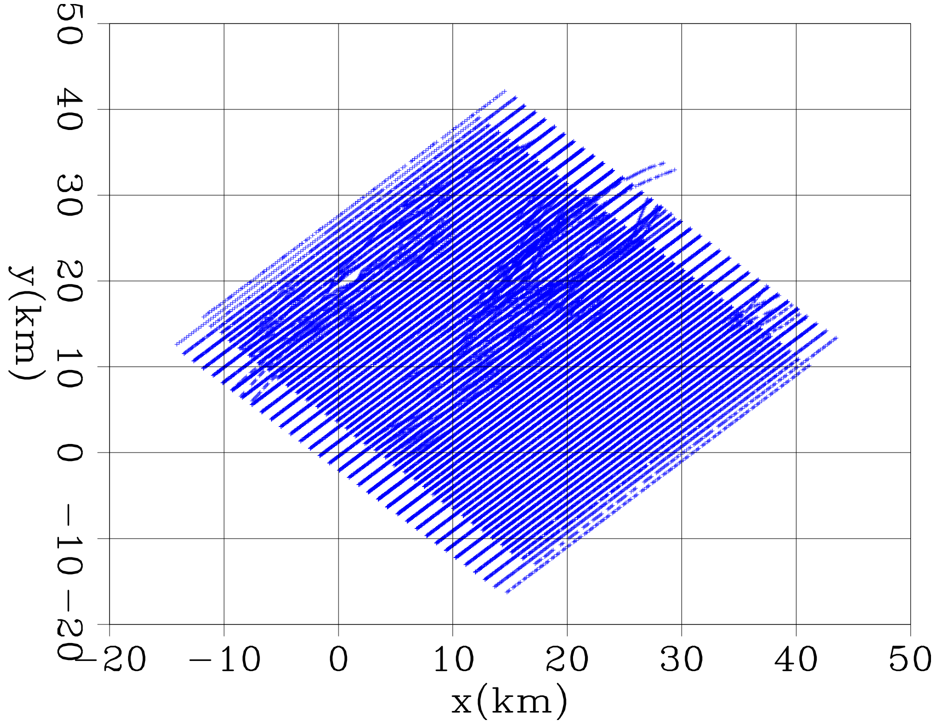

(a)

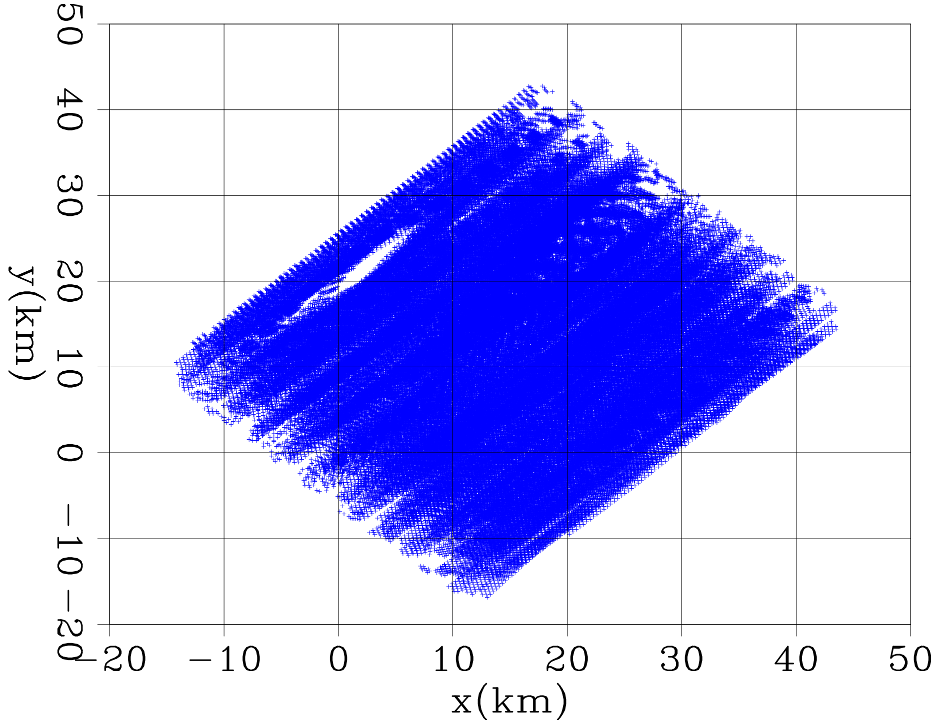

(b)

Figure 4: The total source (a) and receiver (b) coverage in the survey. From the shot locations, we can clearly see the two kinds of sail-lines in opposite directions. [**ER**]

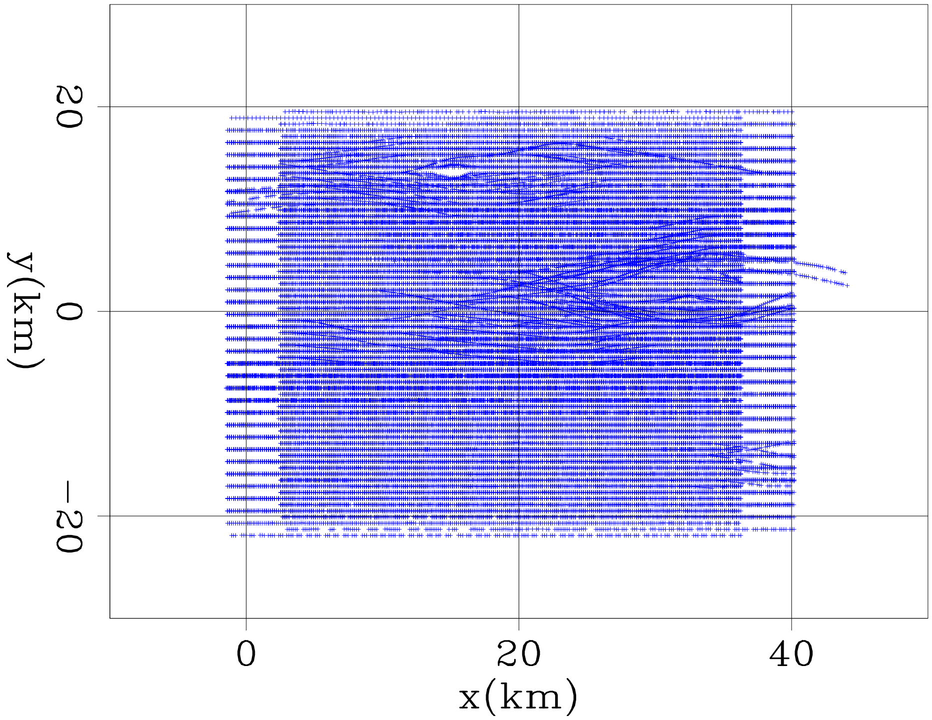

Figure 5: The shot locations map after the applying the geometric transform. [**ER**]

contain 5 axes: time, inline offset, crossline offest, shot location inline, and shot location cross-line. The actual axis parameters in the data grids determine the final size of the regularized data set. If we use the exact parameters from the nominal acquisition geometry described above, the regularized data size reduces to ∼7.9 TB.

- Given our target imaging resolution, we increase the inline receiver spacing from 12.5 m to 25 m. This reduces the data size by half, to ∼3.9 TB.
- The entire shot locations map covers about an area about 40 km by 42 km, but our velocity model's dimension is only about 34 km by 35 km. We discard the shot-receiver locations that are far away from this region, and we further throw away the shots on the edge of the shot locations map that have very poor illumination folds(bin counts). This further reduces the data size to ∼1.9 TB.
- To reduce the total number of shots, we group the shot gathers fired by all 4 source vessels at nearby locations (<75 m inline) into one supergather for each shot location. This reduces the total number of shots by a factor of 4.

Finally, the regularized data set reduces to ∼1.9 TB, containing ∼8,000 shots.

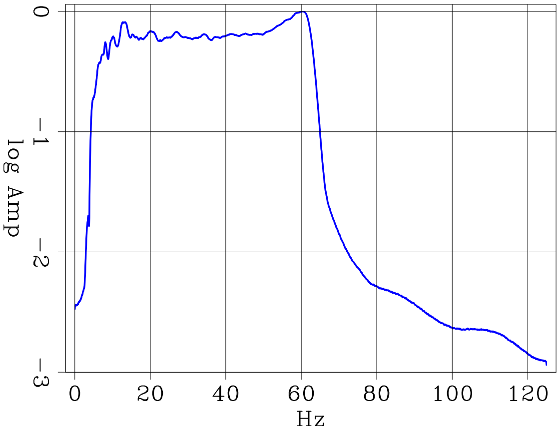

Figure 6: The average spectrum (log scale) of a typical shot gather. The frequency range containing significant energy is about [5 Hz, 70 Hz]. [**CR**]

DATA PREPROCESSING

The original data we received from Schlumberger has already gone through many data processing steps. Some noteworthy ones include low-cut noise filtering, source de-bubble and src/recv deghosting, as well as surface multiples removal. Figure 6 shows the frequency spectrum of a typical shot gather, in which the frequency range containing significant energy is about [5 Hz, 70 Hz]. However, by examining the time-domain data at different frequency bands, we find that the maximal usable frequency is no higher than ∼48 Hz because the data is contaminated by some type of coherent, checkerboard-pattern noise above 48 Hz.

Because we aim at imaging deep subsalt target, we apply water-bottom mute to remove the refracted energy and some processing artifacts that appear above the water-bottom reflection. We also apply t-power gain (power=2.4) on the data to compensate for geometric spreading and medium attenuation. These steps turn out to be very helpful for imaging deeper regions.

INITIAL MIGRATION IMAGES

Figure 7 shows the best velocity model we received from Schlumberger. According to the processing report, this model is the final result of a comprehensive velocity analysis workflow, including a multi-azimuth tomography on the sediment velocity above the salt body, one sediment flooding/migration and two rounds of salt flooding/migration for the salt interpretation, and finally a “slow gradient” revision on subsalt areas. Figure 7(a) and 7(b) demonstrate the 2-D sections of the same model with at different slicing coordinates. There are strong lateral variations along both X and Y directions, therefore the 3-D wave propagation effect would be very prominent, rendering any effort to analyze an individual 2-D portion of the data ineffective (illustrated in the next subsection).

We use one-way WEM method to migrate the data set, so we convert the time domain data to the frequency domain. To further reduce the amount of computation

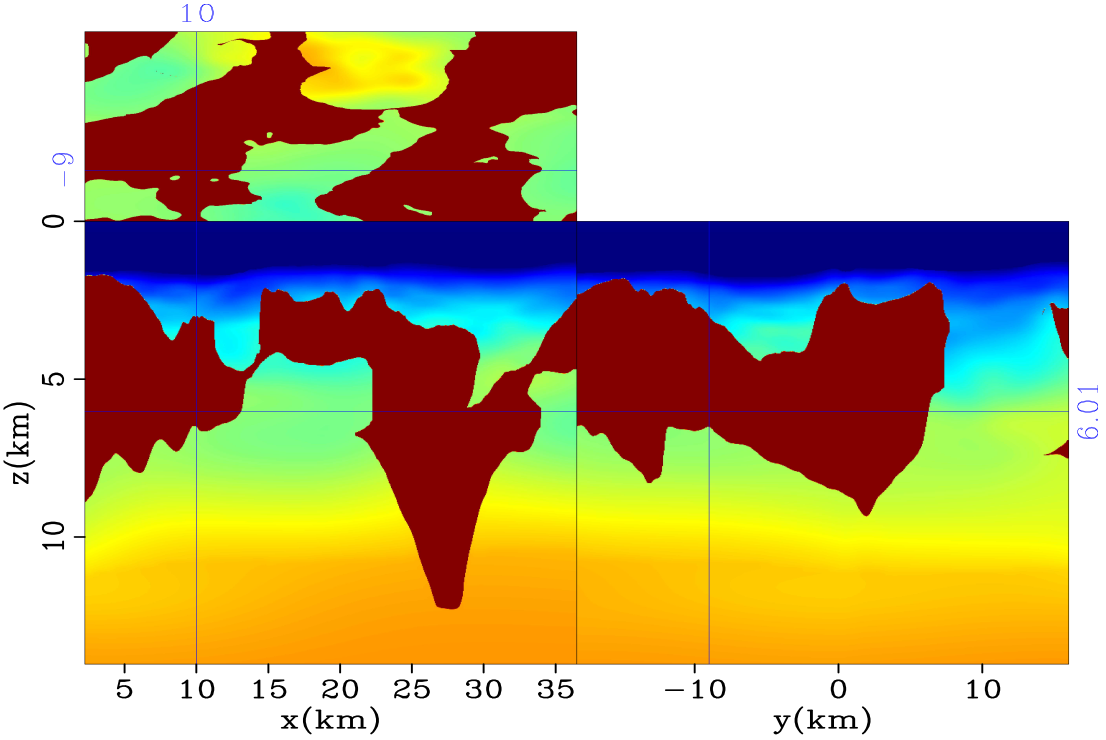

(a)

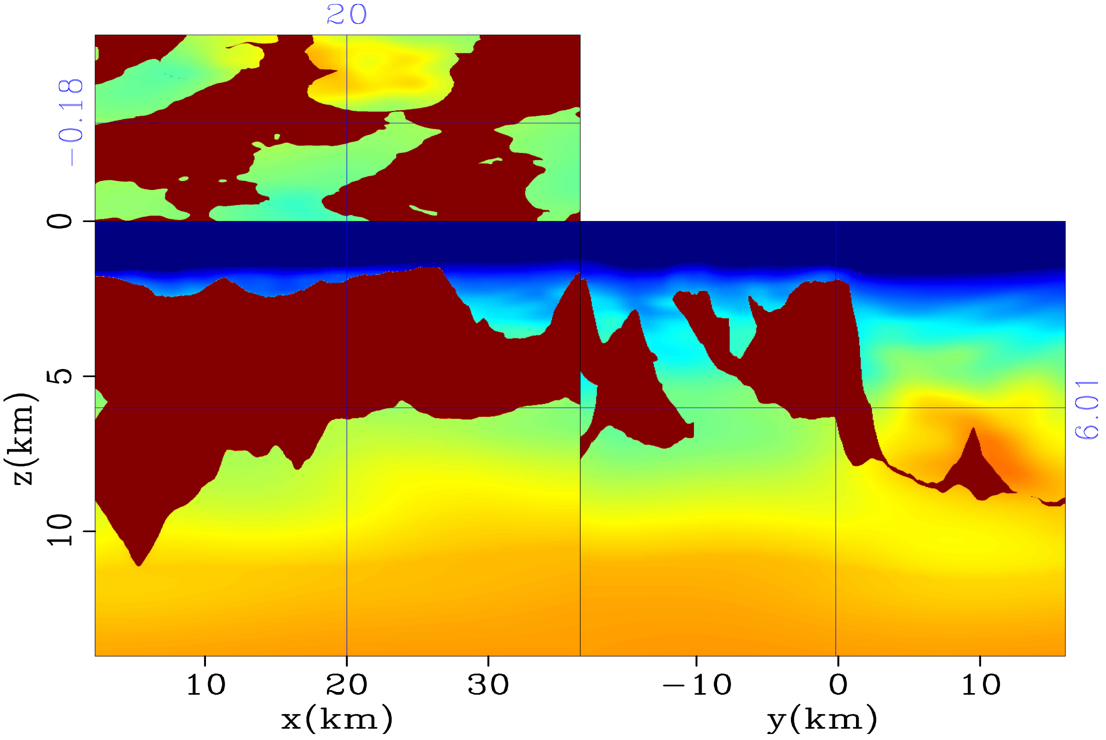

(b)

Figure 7: Three-panel display of the velocity model used for migration, subplot (a) is sliced at x=10 km,y=−9 km, subplot (b) is sliced at x=20 km,y=−0.99 km. Notice the strong model variations along both X and Y directions. The color map ranges from 1450 m/s (deep blue) to 4480 m/s (deep red). [**ER**]

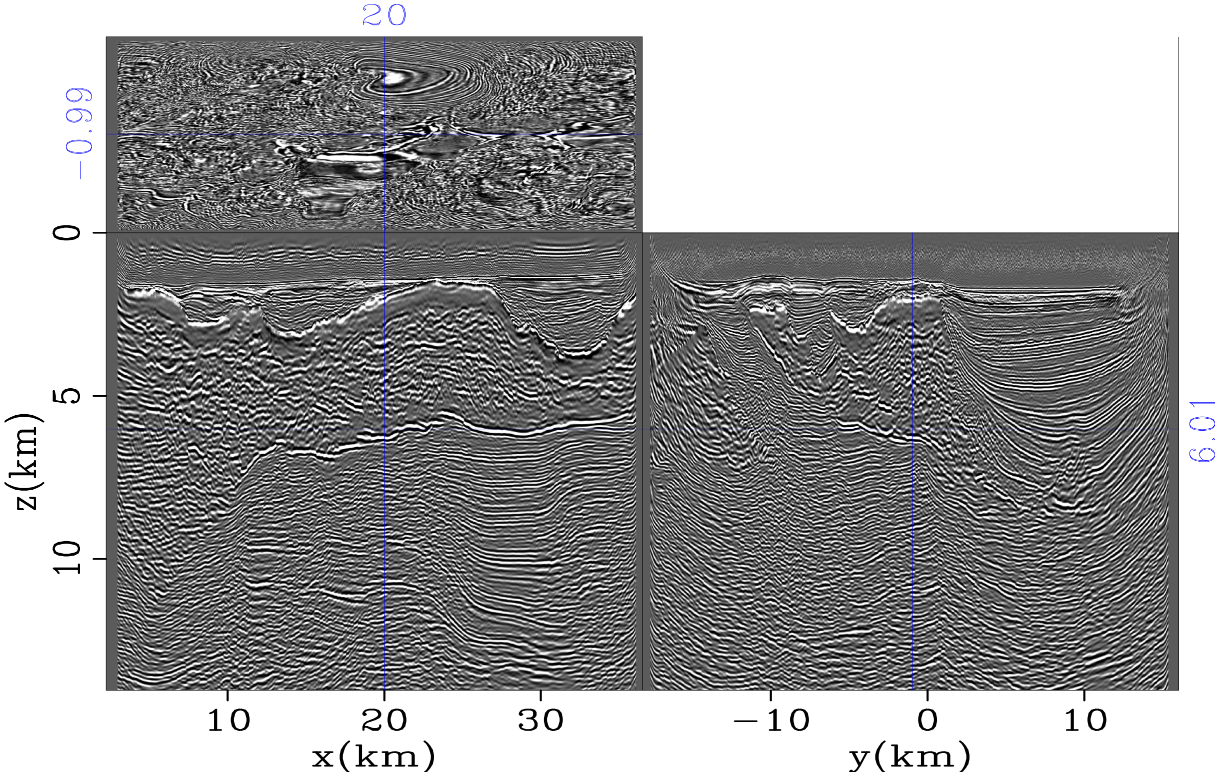

Figure 8: 3-D seismic image migrated with the regularized data set using the velocity model shown in figure 7. An AGC of 1.2 km windows size in Z is applied. [**CR**]

required, we decide to use only ∼200 frequency slices in the range of [5 Hz,20 Hz], after considering the following factors: 1) the usable frequency band; 2) the desired spatial resolution of the image; and 3) the total length of time record required to image the target depth. The spacing of the imaging grid we use is 25 m(X) by 30 m(Y) by 20 m(Z).

Figure 8 shows one section of the full 3-D migrated image. As we can see from the figure, the image quality of the sediments above the salt is very good, with continuous and coherent reflector geometries, which is an indication of accurate velocity. However, the subsalt areas are not as well imaged. There are many discontinuities in the reflectors, as well as conflicting dips. These are indications of a less accurate velocity model. We try to focus our efforts in these regions.

2-D vs. 3-D image comparison

The strong variations of the subsurface model along both inline and crossline directions underline the necessity of using a truely 3-dimensional physical model to analyze this data set. Figure 9 verifies this point by showing the comparison between the results of using 2-D migration and 3-D migration on this data set. The 3-D image is

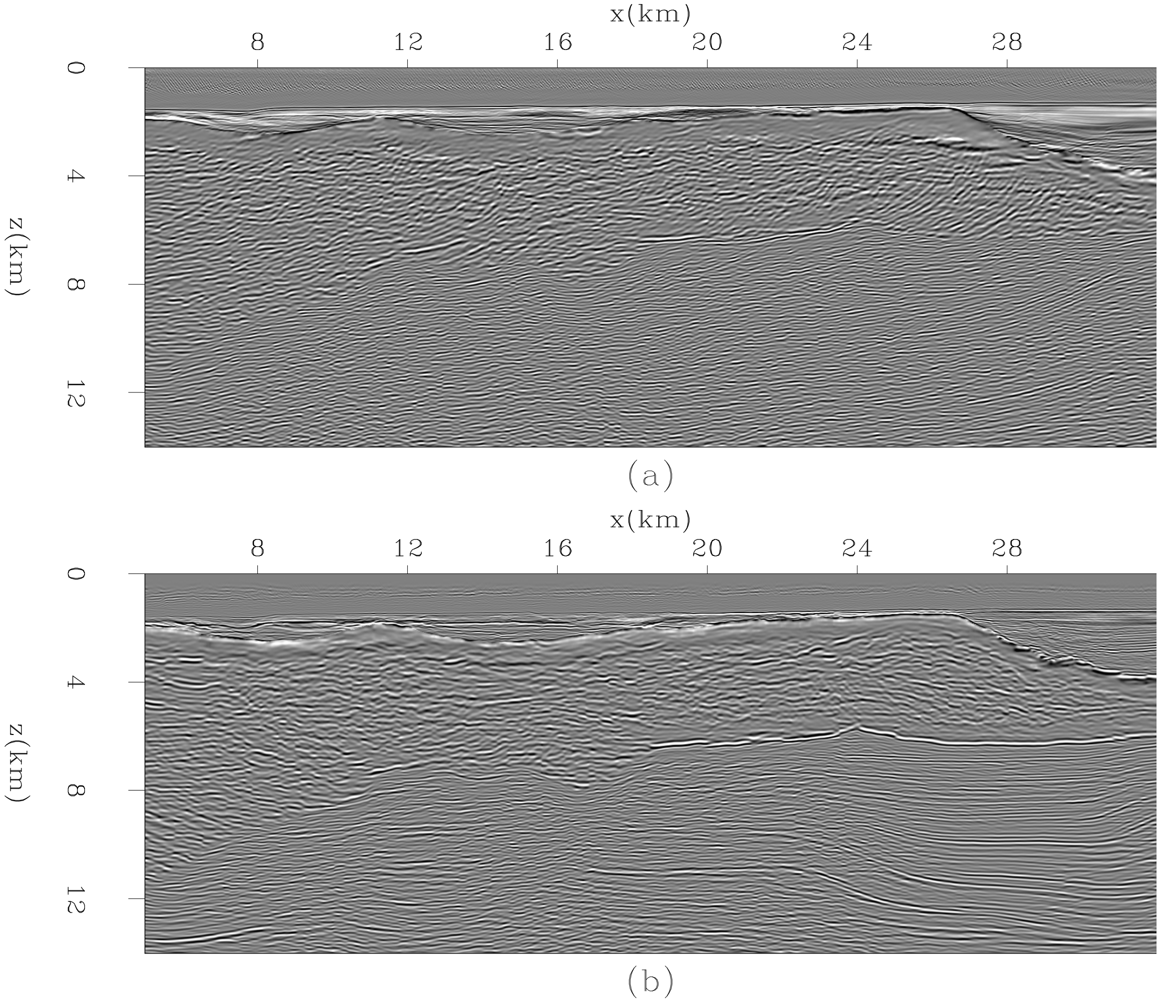

Figure 9: Comparison between an inline section of 2-D migration image (a) and 3-D migration image (b) at the same crossline location ($y = -0.3\,\text{km}$). The 2-D migration uses the single shotline data at $y = -0.3\,\text{km}$. [**CR**]

significantly better than the 2-D image, especially in the subsalt region, where many layering structures observed in the 3-D image cannot even be identified from the 2-D image.

FOCUSING ON SUBSALT SEDIMENTS WITH TARGET-ORIENTED APPROACH

One of the biggest issues in applying WEMVA to such a big data set is the prohibitively high computational cost. Even with all the precautions we make in the data preparation stage, on our academic cluster of 120 Intel Xeon nodes (E5520, 2.26 GHz, quad-core), the full migration on the entire domain (like figure 8) would cost ∼5000 node×hours. It amounts to ∼40 consecutive hours at 100% cluster usage

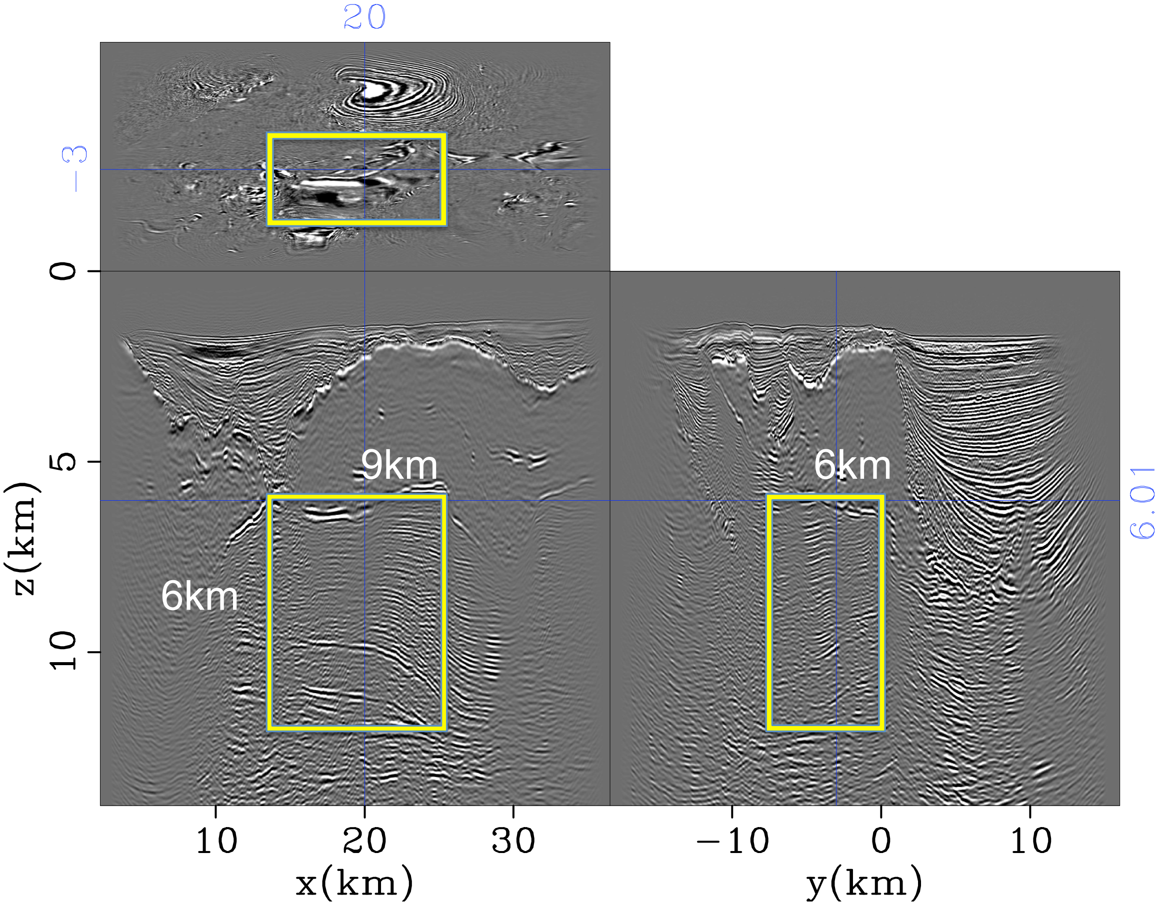

Figure 10: A three-panel view of the initial full 3-D image, in which the region of interest (ROI) for our target-oriented inversion is marked. The image has been applied a z-power (similar to t-power) gain in order to boost up the amplitudes of deeper reflectors. The dimension of ROI is 9 km by 6 km by 6 km. [**CR**]

in an optimal case. In practice, it takes us at least 5 days to complete a job like this.

The turn-around time would be too long for a practical application, given that the wave-equation tomographic operator is even more expensive than the imaging operator, and that we have to perform tens of iterations in a typical WEMVA inversion. In the previous section, we reduce computation by focusing in the data-domain. Fortunately, further reduction can be achieved in the model domain, i.e. we can apply our WEMVA inversion only to the part of model that we are mostly interested in. In our example we would like to choose a subsalt region, because subsalt areas on one hand are very challenging for model estimation due to the complexity of wave propagating through salt body; on the other hand, subsalt regions often contain host structures for oil&gas reservoirs, therefore enhancing subsalt images brings potentially significant economic interest.

The target area we chose is a 9 km by 6 km by 6 km subsalt sediment region in the

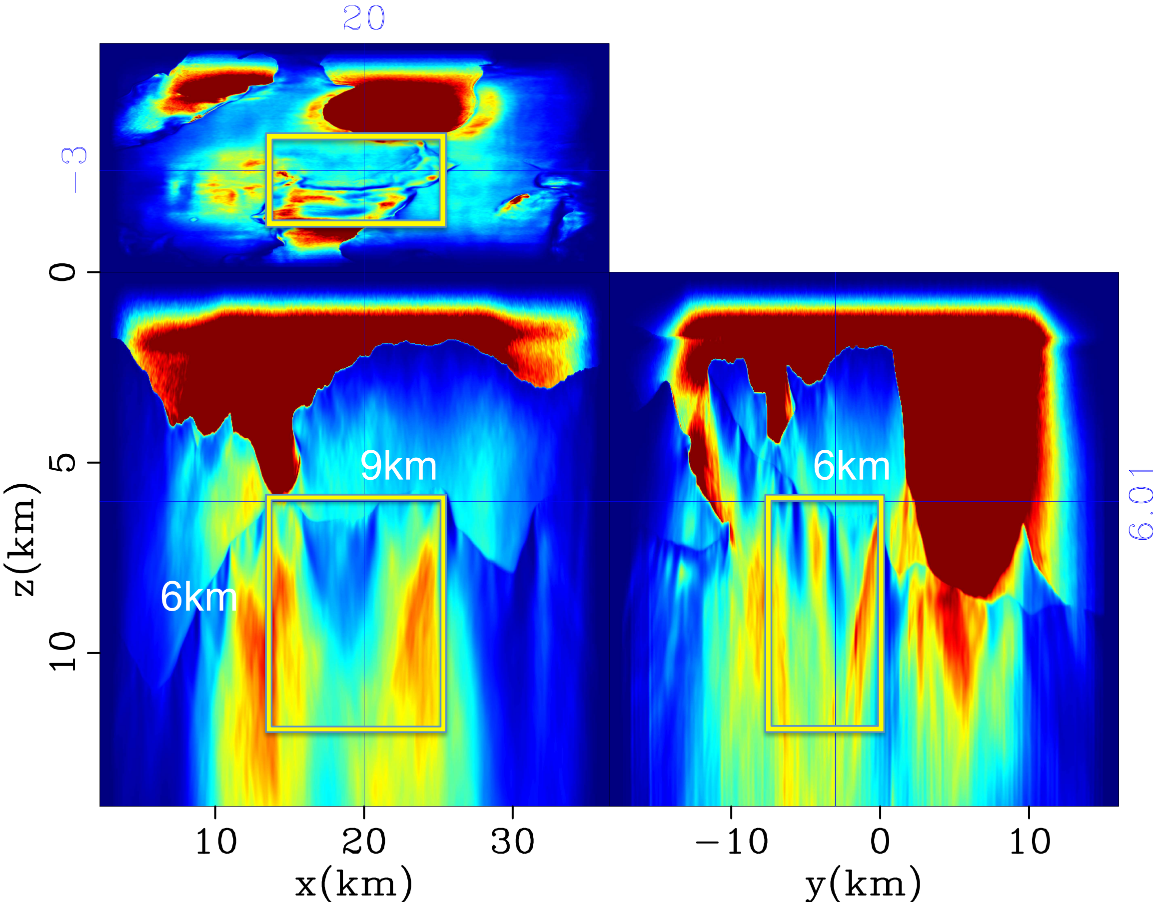

Figure 11: A three-panel view of the 3-D imaging Hessian (diagonal) under the original acquisition setting, in which the region of interest (ROI) for our target-oriented inversion is marked. The Hessian cube has been applied a z-power (similar to t-power) gain in order to boost up the amplitude of deeper region. [**CR**]

middle of our imaging domain, as shown in figure 10. We considered this area a good target for WEMVA-based velocity improvement because there a lot of discontinuities among the imaged sediment layer interfaces, which indicates inaccurate medium velocity. Additionally, the salt overburden above this region is relatively well imaged, therefore we have confidence on the correctness of the salt body model. This leads us to believe that the velocity errors mainly exist within the subsalt sediments, and our WEMVA method is good at resolving this type of velocity errors. Finally, the relatively simple salt overhang enables enough amount of seismic energy to pass through and illuminate the target area, as demonstrated by figure 11 — the diagonal imaging Hessian computed using random-phased encoding approximation (Tang, 2008). The diagonal Hessian is equivalent to a source-receiver illumination indicator, and from the figure we can see that there is reasonable amount of illumination (although quite uneven) for the entire target region.

Initial 3-D common image gathers in the target region

A solid way to verify the existence of velocity error in the target region is to compute the common image gathers. We compute the subsurface-offset gathers (both in h_x and h_y) for the target region. For the range of the offset axes, we found that we need to use 21 points in h_x with 50 m spacing and 19 points in h_y with 60 m spacing in order to capture most of the unfocused energy. Computing these gathers is very I/O intensive because our gathers are almost 400 times size of our image. Our measurement shows that computing these gathers takes twice amount of time compared to computing an image without gathers. Fortunately the cost is still manageable, thanks to the fact that we only compute gathers in the target area.

Figure 12 shows an example of the subsurface offset CIGs within an inline image section ($y = -3.51\,\mathrm{km}$), due to the plotting limitation (it is difficult to plot (h_x, h_y) surfaces on paper), we only show a h_x section (while h_y=0) and a h_y section (while h_x=0). As we can see from the figure, there are plenty of unfocused energy in the offset CIGs, partially this is attributed to the very limited range of illumination angles, nonetheless all the curved events in the CIGs clearly indicates the inaccuracy of the velocity model. Figure 13 shows an example of the subsurface angle CIGs within an inline image section ($y = -3.51\,\mathrm{km}$). The exact way of computing 3-D ADCIGs is very time consuming, here for illustration purpose only, we compute the angle gathers approximately by applying 2-D offset to angle transform on corresponding h_x and h_y gathers in figure 12. Notice the very limited range of angular illumination (less than 25°) on both inline and crossline angle gathers. This is mainly a combined result of a complex salt overburden, our relatively short shot-receiver offset and the fact that target region is deep. Nonetheless, there are still many curved events in the ADCIGs, which our RMO WEMVA method will be able to utilize for velocity improvement.

FUTURE WORK

We plan to use the seismic data remapping approach proposed by Tang (2011) for our target-oriented inversion, with which we can synthesize a new data set right above the target zone with desired acquisition geometry by performing born modeling on the initial subsurface gathers. By doing this, we further reduce the data size and the propagation domain. And we will test our RMO-based WEMVA method on the synthesized data set. We will also test the effectiveness of our accelerated (based on compressed-sensing) version of RMO WEMVA (Zhang et al., 2013) on this data set.

CONCLUSION

We presented our efforts on applying our RMO-based WEMVA method to an industry scale 3-D marine WAZ data set — E-Octopus III in the Gulf of Mexico. By doing careful data regularization and preprocessing, and focusing on a relatively small

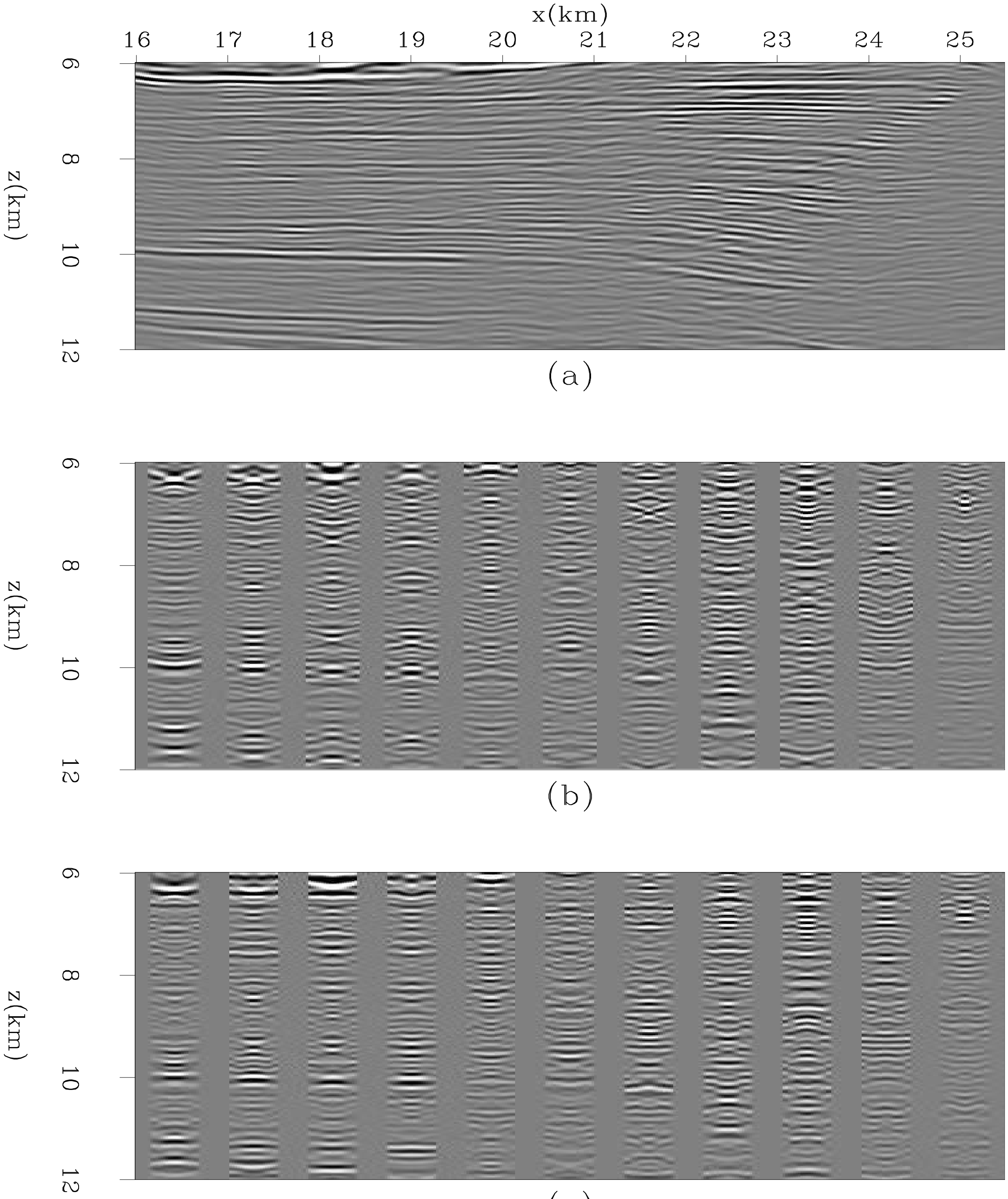

Figure 12: A close-up view of the images and subsurface offset domain common image gathers at the target region of interest (10). (a): An inline image section at $Y = -3.51\,\text{km}$; (b): The inline subsurface-offset (h_x range spans $[-0.50\,\text{km}, +0.5\,\text{km}]$) CIGs for different lateral locations in (a); (c): The crossline subsurface-offset (h_y range spans $[-0.54\,\text{km}, +0.54\,\text{km}]$) CIGs for different lateral locations in (a). [**CR**]

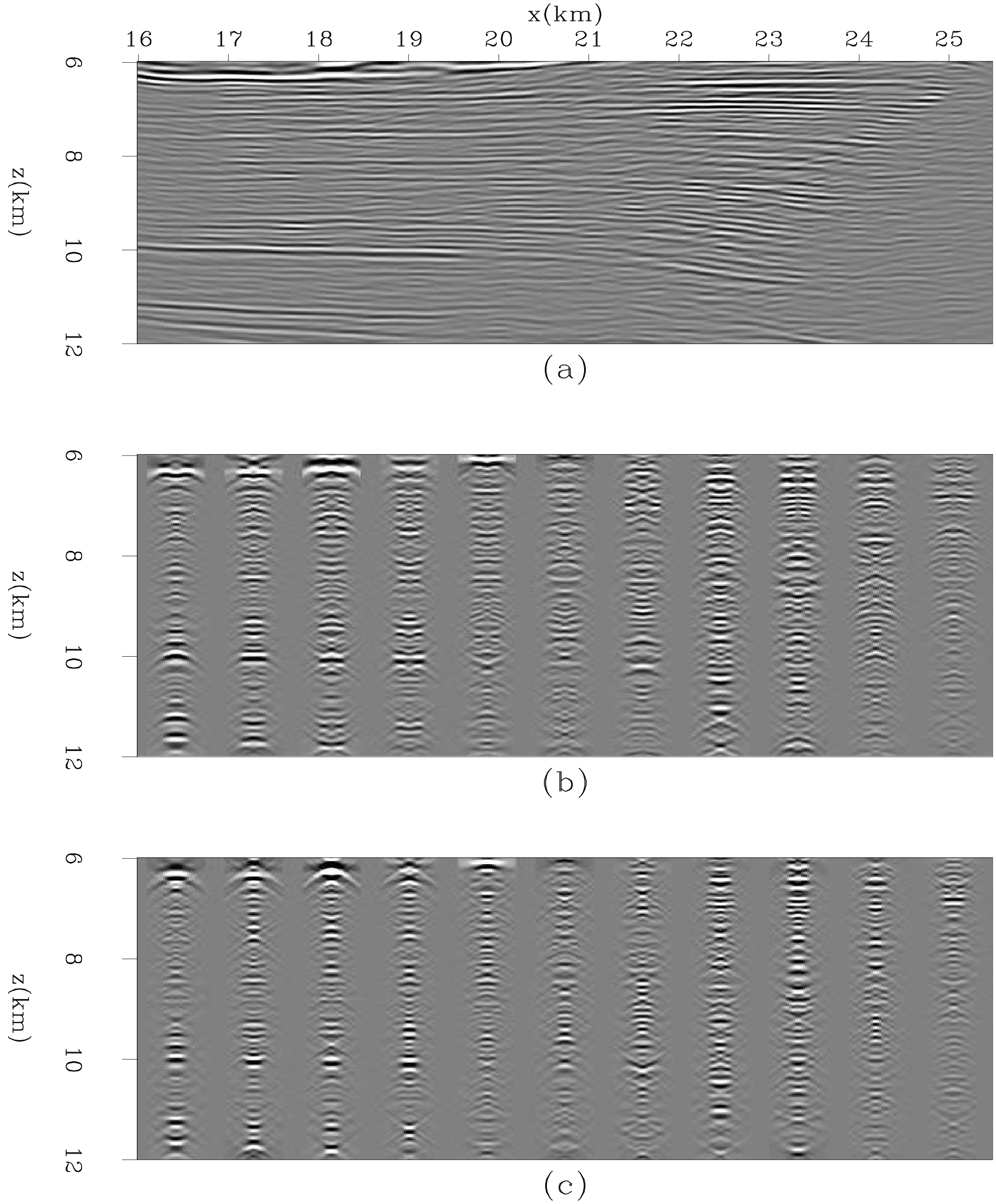

Figure 13: A close-up view of the images and subsurface reflection angle domain common image gathers(approximated) at the target region of interest (10). In this plot, these angle gathers are computed approximately with 2-D offset to angle transform on corresponding h_x and h_y ODCIGs. (a): An inline image section at $Y = -3.51\,\mathrm{km}$; (b): The inline reflection angle (γ range spans $[-35°, +35°]$) CIGs for different lateral locations in (a); (c): The crossline reflection angle (γ range spans $[-35°, +35°]$) CIGs for different lateral locations in (a). [**CR**]

target area containing mainly subsalt sediment layers, we are able to keep the total computation load manageable on our 120 nodes shared academic cluster. Although the angle gathers in the target area have very limited range, we are able to observe clear moveout information from those gathers, which leaves open the opportunity for applying the RMO-based WEMVA for velocity updates.

ACKNOWLEDGEMENTS

We are grateful to Schlumberger for providing this WAZ data set and for permission to publish this work. We thank Stanford's Center for Computational Earth & Environmental Sciences for the computation resources. Our acknowledgements also go to Bob Clapp, Dave Nichols, Elita Li and Yaxun Tang for the technical help and valuable suggestions.

REFERENCES

Biondi, B. and P. Sava, 1999, Wave-equation migration velocity analysis: SEG Technical Program Expanded Abstracts, **18**, 1723–1726.

Chavent, G. and C. A. Jacewitz, 1995, Determination of background velocities by multiple migration fitting: Geophysics, **60**, 476–490.

Tang, Y., 2008, Wave-equation hessian by phase encoding: SEG Technical Program Expanded Abstracts, **27**, 2201–2205.

———, 2011, Imaging and velocity analysis by target-oriented wavefield inversion: PhD thesis, Stanford University.

Zhang, Y. and B. Biondi, 2012, Residual moveout-based wave-equation migration velocity analysis in 3-D: SEP-Report, **147**, 27–38.

Zhang, Y., B. Biondi, and R. Clapp, 2013, Accelerating residual-moveout-based wave-equation migration velocity analysis with compressed-sensing: SEP-Report, **149**, 95–106.

Zhang, Y., B. Biondi, and Y. Tang, 2012, Residual moveout-based wave-equation migration velocity analysis: SEG Technical Program Expanded Abstracts, **31**.